Research Square

Preprints are preliminary reports that have not undergone peer review.
They should not be considered conclusive, used to inform clinical practice,
or referenced by the media as validated information.

A Sequential Multi-Physics Inversion Framework for Cross-Borehole Seismic and Electromagnetic Joint Imaging of Submarine Gas-Hydrate Reservoirs

Amir Yazdanpanah
University of Tehran
Maysam Abedi
maysamabedi@ut.ac.ir
University of Tehran

Research Article

Keywords: Gas-Hydrate Reservoirs, Fracture-Filling, Pore-Filling, Seismic, Electromagnetic Technique, Inversion

Posted Date: May 22nd, 2026

DOI: https://doi.org/10.21203/rs.3.rs-9598347/v1

License: This work is licensed under a Creative Commons Attribution 4.0 International License.
Read Full License

Additional Declarations: No competing interests reported.

Version of Record: A version of this preprint was published at Acta Geodaetica et Geophysica on October 13th, 2026. See the published version at https://doi.org/10.1007/s40328-026-00532-2.

A Sequential Multi-Physics Inversion Framework for Cross-Borehole Seismic and Electromagnetic Joint Imaging of Submarine Gas-Hydrate Reservoirs

Amir Yazdanpanah[1], Maysam Abedi[1*]

1- School of Mining Engineering, College of Engineering, University of Tehran, Tehran, Iran

*Corresponding author: maysamabedi@ut.ac.ir

Abstract

Subsurface characterization of gas-hydrate reservoirs is crucial for global energy potential, but requires accurate imaging of highly variable and complex structures, such as co-existing pore-filling and fracture-filling hydrates. The resolution required to delineate these structures is often challenging for single geophysical methods, particularly the diffusive electromagnetic (EM) technique. While seismic methods offer high resolution, and EM methods provide sensitivity to hydrate saturation, fully integrated imaging of both properties, especially at sharp structural boundaries, remains an unresolved problem. This paper sets out to validate a novel workflow that uses structurally constrained multi-physics inversion to leverage the high resolution of seismic models, specifically first-arrival traveltime and amplitude attenuation, to sharpen the resolution of the electrical resistivity model for complex gas-hydrate geometries. Three synthetic reservoir models (Fracture-Filling, Pore-Filling, and Composite) were created for forward modeling. The inversion utilized an unstructured finite element mesh, optimized based on the Gauss-Newton inversion scheme, and solved iteratively using the Conjugate Gradient Least Squares (CGLS) method. Despite the fact that the unconstrained initial inversions didn't struggle to resolve sharp boundaries for seismic approaches, the resistivity models indicate limitations to recover assumed gas-hydrate geometries. However, the final structurally constrained models successfully recovered the distinct geometric features of all three scenarios, including the localized deep anomaly and the laterally extensive shallow layer, achieving robust statistical fits ($\chi_N^2 \approx 1$ and rRMS error < 10%). The final models validate the effective transfer of structural information from the seismic domain to the diffusive EM domain. This approach provides a significant advancement in the reliable characterization and delineation of complex, multi-geometry gas-hydrate accumulations, offering a critical tool for detailed reservoir assessment and exploration planning.

Keywords: Gas-Hydrate Reservoirs, Fracture-Filling, Pore-Filling, Seismic, Electromagnetic Technique, Inversion.

1. Introduction

Gas hydrates represent naturally occurring, ice-like compounds formed from water molecules encasing gas, predominantly methane, under specific pressure and temperature conditions prevalent in marine and permafrost environments (Ruppel, 2018). These deposits occur primarily in polar regions associated with permafrost and in deep ocean sediments beyond 300-500 meters water depth, where they harbor an estimated carbon volume roughly twice that of all conventional fossil fuels combined (Collett, 2001). Their multifaceted importance draws scientific attention across energy resource potential, contributions to global climate dynamics through methane release, and influences on seafloor stability during geological processes (Kvenvolden, 1993). Despite this promise, substantial technical hurdles persist in extraction and utilization, necessitating advanced investigative approaches to overcome environmental and operational complexities (Moridis et al., 2011).

Marine gas hydrate accumulations manifest in distinct forms, broadly categorized as deep-seated stratigraphic deposits and shallower structural types often linked to gas chimney features, with the latter showing particular viability for production (Matsumoto, 2009). Fracture-filling gas hydrate (G.H.F) emerges within near-vertical fractures in unconsolidated fine-grained sediments, extending over meters and influenced by factors such as methanogenesis, methane solubility, fluid flow variations, and formation kinetics modulated by disturbance rates or chemical promoters (Brunet et al., 2025). In contrast, pore-filling gas hydrate (G.H.P) occupies sediment pore spaces, forming connected three-dimensional networks that provide mechanical reinforcement and dramatically reduce permeability, especially in quartz sands and arenite sandstones, with effects varying by saturation levels and directional orientations (Guan et al., 2024; Lei et al., 2022).

Geophysical investigations have emerged as the cornerstone for detecting, characterizing, and differentiating gas hydrate morphologies in marine sediments. Seismic reflection surveys, particularly through the identification of bottom-simulating reflectors and anomalous velocity increases, have traditionally provided the first indirect evidence of hydrate presence, while controlled-source electromagnetic methods exploit the pronounced resistivity contrast induced by hydrate saturation (Hyndman et al., 2013; Weitemeyer et al., 2006). Integrated analyses of P-wave velocity and electrical resistivity have proven especially powerful for discriminating fracture-filling from pore-filling hydrates, as the former typically exhibit markedly higher resistivity yet lower compressional-wave (P-Wave) velocity at equivalent saturation levels, yielding distinct signatures in cross-plots that enable morphological identification and quantitative saturation estimation (Liu et al., 2020). Such joint approaches, validated in permafrost settings through coupled geophysical-geothermal schemes that predict hydrate saturation from elastic wave velocities and effective thermal conductivity, highlight the complementary nature of elastic and electrical properties in resolving ambiguities where single-method techniques fall short (Vasheghani Farahani et al., 2021).

To achieve the high-resolution imaging required for complex marine hydrate reservoirs, this study employs three specific tomographic techniques. The first implemented method is first-arrival traveltime tomography. Seismic traveltime tomography is a non-destructive imaging technique that generates cross-sectional pictures of geological structures by analyzing seismic wave travel times

through subsurface media (Shi & Wang, 2024). This method has evolved from traditional ray-based approaches to advanced wave-equation methods, which establish linear relationships between traveltime residuals and velocity perturbations using finite-frequency sensitivity kernels (Taillandier et al., 2009; Tong et al., 2014). For large datasets, modern implementations prioritize computational efficiency through gradient-based algorithms, often leveraging the adjoint-state method, where computational cost is independent of data size (Tryggvason et al., 2009). The complementary technique, seismic amplitude attenuation tomography (AAT), maps energy dissipation within the subsurface, typically quantified by a dimensionless parameter typically called as seismic quality factor Q. AAT is crucial for detecting faults, fractures, and visco-acoustic effects (Quan & Harris, 1997; Watanabe & Sassa, 1996). Recent progress in AAT includes improved centroid-frequency-shift algorithms and the expansion to 3D tomographic methods that compensate for interference factors, providing comprehensive attenuation characterization (Hu et al., 2011; Xin et al., 2008). Finally, electromagnetic (EM) diffusion-time tomography utilizes time-domain EM signals to reconstruct electrical conductivity distributions (Lee & Xie, 1993). This method is particularly effective in conductive marine environments where it transforms the diffusive EM field into an analyzable wavefield. By applying ray tomography to the low-frequency EM data, the minimum diffusion time is used as a robust estimator of average conductivity, offering improved resolution in complex conductivity regions (Yu & Edwards, 1997). These integrated methods, when combined, offer a powerful suite for detailed reservoir characterization.

Among the various configurations, cross-borehole geophysical techniques offer particularly high resolution for imaging the shallow to intermediate subsurface where most exploitable hydrate accumulations reside. Cross-hole seismic traveltime and attenuation tomography, combined with electrical resistivity and low-frequency electromagnetic surveys, have demonstrated superior capability to delineate thin hydrate-bearing layers and fracture networks that are frequently below the detection threshold of surface-based methods (Miyairi et al., 1999; Pratt et al., 2003). Recent developments in cross-hole electromagnetic resistivity tomography simulation frameworks, capable of distinguishing high-resistivity targets through optimized electrode configurations and 3D modeling of borehole-to-surface responses, address ongoing challenges in precise reservoir characterization within complex geological formations (Liu et al., 2022; Omisore et al., 2022). These evolutions, building on decades of progress from early resistivity profiling to integrated multi-parameter studies, collectively advance the refinement needed for reliable assessment of hydrate morphology, resource potential, and production feasibility in marine environments (Bialas et al., 2020; Riedel et al., 2010).

Despite significant progress in geophysical imaging, the accurate characterization of morphologically complex gas-hydrate reservoirs—especially those containing thin fracture networks or coexisting pore- and fracture-filling hydrate facies—remains a persistent challenge when relying on single-method approaches. To address this limitation, this study introduces a sequential multi-physics imaging workflow. First, independent inversions of seismic traveltime and amplitude attenuation data are performed on fully unstructured triangular meshes, producing high-resolution P-wave velocity and attenuation models that robustly resolve stratigraphic layering and key structural geometries. These seismically derived results are then employed as a geologically consistent structural prior to inform a subsequent inversion of electromagnetic

diffusion time data. This third-stage, structurally constrained inversion capitalizes on the distinct sensitivity of electrical resistivity to hydrate occurrence mode, whether pore-filling or fracture-hosted, while preserving lithological boundaries that conventional regularization techniques tend to oversmooth (Fig. 1).

Any geophysical inversion inherently struggles with ambiguity and diminishing resolution, particularly with increasing depth. To mitigate this issue, structural information can be integrated to provide valuable constraints on sharp geological boundaries within the subsurface. This structural information is typically derived from wave-based methods that naturally offer superior resolution, such as seismic surveys (Tanner et al., 2020), ground-penetrating radar (Doetsch et al., 2012; Jiang et al., 2020), or discrete data from boreholes (Wunderlich et al., 2018). These constraints can be applied as boundary conditions, whether extracted from 2D lines (Jiang et al., 2020) or 3D facets (Doetsch et al., 2012), enabling the inversion of less-resolved parameters (like electrical resistivity) to honor the sharp structural features identified by the high-resolution survey (like seismic P-wave velocity).

Building upon the established forward modeling capabilities of the pyGIMLi library, which provides a robust ray-based shortest path operator for seismic refraction traveltimes, we have developed two novel forward operators specifically tailored for cross-borehole applications. The first operator extends the framework to model seismic amplitude attenuation with a visco-acoustic frequency-domain approach, while the second formulates the propagation of electromagnetic waves in the diffusive regime. These operators were implemented through rigorous mathematical conversions that translate the original ray-tracing kernel into physically consistent formulations for amplitude decay and EM diffusion, as detailed in the Methodology section. In this work, we systematically examine the performance of these operators by simulating three distinct physical parameter datasets—P-wave traveltime, amplitude attenuation (quality factor Q), and electromagnetic diffusion time—across three different cross-borehole subsurface scenarios. All simulations are performed on high-resolution unstructured triangular meshes that accurately honor borehole geometries and stratigraphic interfaces. Following the generation of these synthetic datasets, we carry out independent inversions for each parameter. Subsequently, we investigate the potential for improving electromagnetic inversion results by imposing structural constraints derived from the two seismic models. This sequential multi-physics strategy aims to transfer the high-resolution structural information inherent in seismic models to guide and regularize the inherently smoother electromagnetic inversion, thereby enhancing the delineation of complex hydrate morphologies.

2. Methodology

This section outlines the numerical framework developed for the sequential multi-physics imaging workflow. Forward modelling of seismic and electromagnetic responses is performed on high-quality unstructured triangular meshes that favor the acquisition geometry and known stratigraphic boundaries. Inversion is conducted in two stages: first, independent smoothness-constrained reconstruction of seismic velocity, amplitude attenuation, and EM diffusion times; second,

structurally constrained inversion of EM diffusion-time data guided by the seismic results. The following subsections describe the forward operators, and inversion schemes in turn. The main computational framework of this study has been implemented using pyGIMLi open-source library (Rücker et al., 2017). In addition, it is presumed that the cross-hole geophysical surveys are conducted in open holes or within non-metallic casings of the well bore to minimize signal attenuation, particularly for EM waves.

2.1. Forward Modeling

Accurate reservoir characterization fundamentally depends on reliable forward models that precisely simulate the physics of wave propagation and EM diffusion within complex subsurface structures. This requires numerically stable and efficient solvers capable of handling the highly heterogeneous media associated with gas hydrate accumulations, particularly the sharp interfaces between hydrate-bearing fractures and the surrounding sediment.

2.1.1. Seismic P-wave velocity and amplitude attenuation

The seismic forward problem is addressed by computing both first-arrival traveltimes t and amplitude attenuation Q^{-1}, which provide complementary information on elastic properties and energy dissipation. Both are crucial for robust discrimination of gas hydrate morphologies. Traveltimes are computed by solving the Eikonal equation (a high-frequency approximation of the wave equation) using Dijkstra's shortest-path algorithm (Dijkstra, 1959) on a triangular mesh. This approach efficiently calculates the minimum time required for the wave front to propagate from the source to all receiver locations. The unstructured mesh enables accurate representation of sharp geological boundaries and minimizes numerical artifacts that often plague regular grids, particularly in regions of high-velocity contrast.

The traveltime, t, for a single ray propagating through N discrete cells (or model elements) is given by the sum of the traveltimes through each element (Moser, 1991):

$$t = \sum_{i=1}^{N} \frac{l_i}{v_i} = \sum_{i=1}^{N} l_i s_i \tag{1}$$

where l_i is the segment length of the ray within the i-th cell, v_i is the P-wave velocity while s_i is the slowness (reciprocal of velocity, $s_i = 1/v_i$) in that cell. To improve angular coverage and numerical accuracy of traveltime calculations, a few secondary nodes can be applied the corner points (cell edges).

For all ray paths, the forward calculation can be expressed as a linear matrix-vector product:

$$t = \boldsymbol{W}.s \tag{2}$$

where t is the observed traveltime vector, s is the slowness model vector, and $\boldsymbol{W}$ is the modeling matrix (or ray-length matrix) where each element W_{ji} represents the length of the j-th ray within the i-th cell.

The presence of gas hydrates, especially when highly saturated or fractured, introduces significant visco-acoustic effects that cause pronounced energy loss. This loss is quantified by the seismic quality factor Q (defined as the ratio of the energy stored to the energy dissipated per cycle of oscillation, thus it is a dimensionless parameter), where its inverse Q^{-1} (attenuation factor), serves as the inversion model parameter in the case of amplitude attenuation. High Q^{-1} values correspond to high energy loss and strongly suggest hydrate presence, complementing the velocity information.

For a single ray, the amplitude decay, A, is governed by the relation to the source amplitude, A_0:

$$A = A_0 . \exp\left(-\frac{\pi f t}{Q}\right) \tag{3}$$

where f is the dominant frequency of the seismic wavelet. When the ray passes through M discrete elements, the total attenuation is multiplicative across the segments:

$$A = A_0 . \prod_{i=1}^{M} \exp\left(-\frac{\pi f l_i s_i}{Q_i}\right) \tag{4}$$

Taking the natural logarithm of the normalized amplitude (A/A_0) transforms this non-linear product into a linear sum:

$$\ln\left(\frac{A}{A_0}\right) = \sum_{i=1}^{N} \left(-\frac{\pi f l_i s_i}{Q_i}\right) \tag{5}$$

This expression can be rearranged to define the attenuation forward problem in a linear form. If we define the model parameters as $m = \left\{m_i = {}^{1}/_{Q_i}\right\}$, the forward function, $f(m)$, is given by the matrix-vector product:

$$f(m) = \boldsymbol{A}.m = \boldsymbol{W}.diag(-\pi f s).m \tag{6}$$

Here, $\boldsymbol{A}$ is the effective attenuation modeling matrix, constructed from the ray-length matrix $\boldsymbol{W}$, the frequency f, and s is the previously inverted slowness model. The s values are derived from the traveltime inversion, making the attenuation inversion dependent on the velocity model. As a result, the seismic process can be assumed as a sequential framework, enhancing the overall resolution while also getting validated to play a very crucial role as a robust structural constraints on other models (Watanabe & Sassa, 1996).

2.1.2. Electromagnetic Geometrical Diffusion Time

The low-frequency EM response in the conductive marine environment is fundamentally governed by the diffusion equation, which characterizes the propagation of the magnetic field H through the

medium. In the absence of displacement currents, this physics contrasts sharply with the wave propagation observed in seismic methods.

In a uniform, 2D medium, the behavior of the magnetic field due to a transient point source is governed by the diffusion equation (Böhm et al., 2015):

$$\frac{\partial H}{\partial t} = D\nabla^2 H + M_0 \delta(t)\delta(x - x_1) \tag{7}$$

Where $D = 1/\mu\sigma$ is the magnetic diffusivity, μ is the magnetic permeability, σ is the electrical conductivity, M_0 is the source strength, and δ is the Dirac delta function applied at the source location x_1 and the time t=0.

The solution to this equation, expressed via Green's function, defines the physical diffusion of the EM energy. For cross-borehole inversion, the complexity of solving the full diffusion equation is circumvented by leveraging the theoretical link to seismic traveltime. This link is derived from the high-frequency asymptotic solution of the diffusion equation, which establishes a direct analogy to Fermat's Principle (Berryman, 1989). Crucially, the path of earliest arrival for the diffusing EM energy can be approximated as the trajectory of minimum diffusion time t_{EM}.

This relationship dictates that the square root of the diffusion time is linearly related to the integral of the reciprocal of the square root of diffusivity along the path from the source x_1 to the receiver x_2:

$$\sqrt{t_{EM}} = \frac{1}{2}\int_{x_1}^{x_2} \frac{dx}{\sqrt{D}} \tag{8}$$

The EM forward operator has been created based on Eq. 8 and assumed resistivity model. In this operator, the magnetic permeability value has been set to $\mu = 4\pi \times 10^{-7}$.

2.2. Multi-Physics Inversion Strategy

The reconstruction of subsurface property models (velocity, amplitude attenuation, and electrical resistivity) from observed data relies on solving a highly non-linear, ill-posed inverse problem. This challenge is addressed through an iterative, regularized approach based on the Gauss-Newton optimization framework. The core of this process is the minimization of a global objective function, $\varphi(m)$, which balances the fidelity of the model to the measured data with the requirement for geological plausibility and stability.

The objective function is composed of two primary components: the data misfit term φ_d, which measures the difference between the observed and predicted data, and the model regularization term φ_m, which incorporates a priori information about the expected model structure. These terms are balanced by the scalar regularization parameter λ:

$$\varphi(m) = \varphi_d + \lambda\varphi_m \longrightarrow min \tag{9}$$

For both the data misfit and the model regularization, the L_2 norm is employed. The L_2 norm penalizes large errors or large variations in the model quadratically, leading to a unique, stable, and smooth solution space. This choice ensures the optimization problem remains convex and amenable to efficient iterative solution found via the conjugate gradient least squares (CGLS) method. The L_2 norm is defined as the square of the Euclidean norm ($\| x \|^2 = \sum x_i^2$), providing a computationally robust metric for minimization (Li & Oldenburg, 1996).

The data misfit term, φ_d, quantifies the disagreement between the observed data d_{obs} and the data predicted by the forward operator $f(m)$ for a given model m. Since the measurements are subject to noise and errors, the misfit is weighted by the inverse of the data covariance matrix, $C_d^{-1/2}$, which incorporates data uncertainties ε_i:

$$\varphi_d = \| C_d^{-1/2}(d_{obs} - f(m)) \|_2^2 \tag{10}$$

$$C_d^{-1/2} = diag(1/\varepsilon_i) \tag{11}$$

The inversion seeks to reduce this term, driving the synthetic data to match the measured data within the bounds of the assigned uncertainties.

The model regularization term, φ_m, addresses the ill-posed nature of the inverse problem by restricting the solution space. This term enforces a measure of smoothness on the resulting model, ensuring stable inversion results and suppressing high-frequency artifacts that are often introduced by noisy data. This study employs a first-order smoothness-constrained Tikhonov regularization (Tikhonov& Arsenin, 1977):

$$\varphi_m = \| W_m(m - m_{ref}) \|_2^2 \tag{12}$$

where W_m is the combined regularization and weighting matrix. Since no explicit reference model is imposed (m_{ref}=0 is implicitly assumed), this term minimizes the model's structural complexity, promoting the 'flattest' structure that fits the data (Günther et al., 2006).

The matrix $\boldsymbol{W}_m$ is further decomposed to incorporate both spatial derivatives and directional weighting:

$$\boldsymbol{W}_m = diag(w_i)C \tag{13}$$

Here, C is the constraint matrix. This matrix represents the spatial derivative operator, specifically a finite-difference operator that minimizes the first spatial derivative (gradient or slope) of the model between adjacent cells. This promotes the smoothest possible reconstruction. Furthermore, $diag(w_i)$ is the directional regularization weighting. This diagonal matrix allows the

regularization penalty to be customized based on direction or geological structure. For all inversions, an isotropic weighting is employed, meaning the penalty applied to model differences between adjacent cells is the same in both lateral (horizontal) and vertical directions. This has mostly been conducted because of the crosswell nature of the designed survey in this study. The magnitude of the weights is dependent on the distance between the cell centers, normalizing the penalty by cell size (Günther & Rücker, 2019; Mollaret et al., 2020). Also, the regularization parameter, λ, is the crucial scalar that controls the trade-off between minimizing the data misfit and the model structure. A large λ heavily penalizes complexity, resulting in a very smooth, stable model that may underfit the data. A small λ emphasizes fitting the data closely, which can lead to unstable, rough models and the amplification of noise. The appropriate λ is typically chosen iteratively, often aiming for a data misfit that equals the expected noise level in the data, thus preventing the over-interpretation of noise. It has been implemented empirically here via parameter sensitivity testing and has resulted in acceptable nearly perfect fits.

The utilized strategy employs a sequential approach, designed to maximize the resolution gained from each geophysical domain (see workflow shown in Fig.1). Seismic slowness and attenuation are inverted separately using the standard isotropic smoothness constraint described above. The resulting high-resolution velocity, and amplitude models are particularly effective at delineating the primary geological layering (i.e., the background structure) and the overall structural boundaries of the hydrate bodies. The final stage EM-based conductivity inversion leverages the structural information from the seismic results to selectively modify the regularization matrix W_m. The seawater layer, presenting the first 300 meters of the geometry domain, has been considered as a single and separated zone throughout all inversions. Physical properties within this zone have been fixed during inversion procedure since no source (transmitters) and receivers assumed on two sides of this layer. This region-specific modification (structural constraining) allows the EM inversion to recover the necessary high-contrast sharp boundaries, sharp physical characteristic of gas hydrate, without applying excessive smoothing regularization across those critical interfaces.

To exploit the computational efficiency of the existing shortest-path solver (developed for seismic traveltimes), the EM problem is transformed into a linear traveltime inversion. This is achieved by defining a new model parameter, *m*, such that:

$$m = \frac{1}{2\sqrt{D}} = \frac{1}{2}\sqrt{\mu\sigma} \tag{14}$$

The forward problem then becomes a linear matrix-vector product operating on the square root of the measured diffusion time $t_{g,\sqrt{}}$, enabling the use of the pre-existing ray length matrix $\boldsymbol{W}$:

$$t_{EM,\sqrt{}} = \boldsymbol{W}.m \tag{15}$$

The inverted model *m* is subsequently used to extract the high-resolution conductivity σ and, thus, resistivity ($\rho = {}^{1}/_{\sigma}$) model, effectively leveraging the inherent sensitivity of electrical properties to the highly resistive gas hydrate zones.

To assess the inversion fit quality statistically, the χ_N^2 parameter has been used which yields the degree of freedom N (i.e., number of data) and can be shown:

$$\chi_N^2 = {}^{\varphi_d}/_{N} \approx 1 \tag{16}$$

3. Synthetic Gas Hydrate Test Reservoirs

The present study systematically evaluates the performance of integrated tomographic techniques in characterizing diverse gas hydrate morphologies by employing three progressively complex synthetic models. These scenarios represent a typical deep-water setting comprising two vertical boreholes separated by 1000 m and penetrating to 2000 m below sea level, with the uppermost 300 m occupied by seawater. Beneath the seafloor, the section is divided into an upper hemipelagic mud-rich sediment layer (300 to 1500 m depth) and a deeper turbiditic silty-sand unit (1500 to 2000 m depth). Figure 2 showcases a detailed schematic of the present study.

The core of this evaluation lies in the distinct elastic (V_p), inelastic (Quality Factor, Q), and electrical resistivity (ρ) properties assigned to each material. The inversion relies on leveraging these complementary sensitivities to differentiate hydrate styles, as the Q factor is crucial for mapping energy dissipation while V_p maps stiffness, and ρ highlights the dramatic electrical contrast induced by hydrate saturation. The specific properties for the background layers (Seawater, Upper Sediment, Deeper Sediment) and the three hydrate scenarios are detailed in Tables 1, 2, and 3. For all three amplitude attenuation scenarios a constant frequency of 50 Hz has been considered which is logical (e.g., a velocity of 2000 m/s would imply a wavelength of 40 m) based on the designed survey geometries.

The first scenario, detailed in Table 1 and depicted in Fig. 3, investigates a single fracture-filling hydrate zone (G.H.F) hosted within the upper mud-rich unit, characterized by sub-horizontal fractures (dip less than 20°) and a significant volume fraction of 0.6. The G.H.F anomaly is expected to exhibit a substantial increase in electrical resistivity alongside a high velocity and low Q signature, making it a target for both electrical and attenuation methods.

The second scenario, summarized in Table 2 and showed in Fig. 4, models a single, horizontally extensive pore-filling hydrate body (G.H.P) located slightly shallower in the same upper sediment unit. This body is modeled with a volume fraction of 0.4. The G.H.P anomaly typically shows a less pronounced resistivity increase than the G.H.F type, alongside an increased V_p and a reduced Q, providing a distinct signature for comparison.

The final scenario, presented in Table 3 and visualized in Fig. 5, tests a composite case containing both hydrate morphologies simultaneously. The G.H.P anomaly is modeled with a higher volume fraction of 0.5 and remains shallower, while the G.H.F anomaly, with horizontal fractures (dip less than 20°) and an increased volume fraction of 0.7, is positioned deeper within the mud-rich layer. This controlled progression of complexity allows systematic evaluation of each geophysical method's ability to detect and distinguish the two end-member hydrate styles under realistic marine acquisition geometry.

The synthetic data sets derived from the simulation of these constructed forward models, which accurately capture the geophysical responses of the modeled reservoirs, serve as the "observed" data for the subsequent joint tomographic analysis.

4. Results and Discussion

The validity of the proposed multi-physics workflow is first examined through the G.H.F. scenario, where the inversion performance is assessed against synthetic data contaminated with 3% random Gaussian noise (Fig. 6). In this simulation, the physical coupling between high-velocity hydrate anomalies and lower attenuation (high Q) was explicitly modeled, a relationship that the inversion successfully recovers as demonstrated by the seismic amplitude ratio predictions. The quality of the data fitting is visualized through absolute misfits for the seismic traveltime and attenuation domains, while relative misfits are utilized for the electromagnetic diffusion times to accommodate the parameter's larger dynamic range. Due to the comprehensive nature of the synthetic setup and the absence of field-data gaps, the inversion algorithms achieved robust convergence, characterized by a $\chi_N^2 \approx 1$ and a relative Root Mean Square (rRMS) error of < 10% across all three physical measurements.

The initial unconstrained inversion results for the G.H.F. scenario are presented in Fig. 7, where panels (a), (b), and (c) correspond to the P-wave velocity (V_p), the seismic quality factor (Q), and the electrical resistivity (ρ), respectively. The traveltime tomography result (Fig. 7a) successfully delineates the high-velocity G.H.F. zone, positioned in the central part of the survey area, and accurately recovers the general trend of the background layering. Correspondingly, the amplitude attenuation tomography (Fig. 7b) effectively images the fracture, showing a zone of lower Q (more dissipative) which aligns with the high-velocity zone, consistent with the expected physical relationship between seismic properties in hydrate-bearing fractured media. Figure 7c shows the primary electrical resistivity inversion result, which was generated using a standard isotropic smoothness constraint. While this ρ model indicates a broad, high-resistivity anomaly corresponding to the hydrate zone, its boundaries are overly smooth, reflecting the limitations of isotropic regularization. These three models serve as the essential starting points for the subsequent structurally constrained inversion, where the structural information from the better-resolved seismic models (V_p, Q) will be later imposed onto the resistivity model.

The data fitting for the G.H.P. scenario (Fig. 8) confirms the robustness of the multi-physics inversion across different target geometries. Unlike the localized anomaly in the G.H.F. case, the G.H.P. model yields broader, shallower patterns in the seismic travel time and amplitude attenuation data, characteristic of a horizontally extensive layer. The observed data (panels a, d, g) is accurately reproduced by the predicted data (panels b, e, h) for all three modalities. The resulting misfit plots (panels c, f, i) for seismic absolute misfit and EM relative misfit are uniformly random, validating that the inversion converged to the 3% noise level. Like the first case, the statistical convergence metrics were exceptionally strong, with $\chi_N^2 \approx 1$ and rRMS error < 10% across all datasets.

Figure 9 displays the initial, unconstrained inversion results for the G.H.P. scenario, providing P-wave velocity (V_p), seismic quality factor (Q), and electrical resistivity (ρ). In contrast to the deep, vertical anomaly recovered in the G.H.F. case, the traveltime tomography (Fig. 9a) successfully delineates the high-velocity G.H.P. zone as a laterally extensive, shallower layer characteristic of pore-filling saturation. The corresponding attenuation map (Fig. 9b) confirms this interpretation by resolving the same horizontal layer as a zone of lower Q (higher attenuation or dissipation), consistent with the expected physical signature. Similar to the previous case, the primary electrical resistivity result (Fig. 9c), generated with isotropic regularization, captures the broad, high-resistivity zone associated with the hydrate layer. While the general location is correct, the inversion result remains overly smoothed and diffusive at the boundaries. These three single-physics models are combined to form the crucial input for the subsequent structural constraint step, aiming to sharpen the poorly-resolved resistivity boundaries using the structural information derived from the seismic data.

Figure 10 presents the multi-physics data, predictions, and misfits for the composite gas-hydrate scenario, which combines the structural features of both the fracture- and pore-filling layer. The observed data (panels a, d, g) now display a superposition of the kinematic and dynamic signatures from both anomalies, demonstrating a more complex pattern compared to the single-feature cases. Crucially, the inversion successfully models this increased complexity, as confirmed by the excellent visual match with the predicted data (panels b, e, h). Consistent with the previous two scenarios, the resulting misfit plots (panels c, f, i) for seismic travel time and attenuation (absolute misfit) and EM diffusion time (relative misfit) exhibit random distributions, confirming that the data was fit to the 3% noise level. This final data fitting exercise validates the ability of the multi-physics forward and inverse models to accurately handle complex reservoir geometries involving simultaneous fracture- and pore-filling hydrate occurrences, while maintaining the high statistical rigor ($\chi_N^2 \approx 1$ and rRMS error < 10%).

The initial inversion results for the composite gas-hydrate scenario, which contains both a deep, narrow G.H.F. zone and a shallower, horizontal G.H.P. anomaly, exhibit the necessity of structural constraints. The P-wave velocity map (Fig. 11a) successfully resolves both high-velocity anomalies simultaneously, clearly delineating the sharp, high-aspect-ratio boundary of the deep fracture and the diffuse, laterally-extensive nature of the shallow layer. This dual-anomaly recovery is mirrored in the attenuation map (Fig. 11b), where both zones are resolved as areas of lower Q (higher dissipation). However, the primary electrical resistivity model (Fig. 11c), produced using standard isotropic regularization, struggles to differentiate these two features effectively. While the plot captures a broad, high-resistivity anomaly corresponding to the combined hydrate presence, the shallow and deep features are blurred together, and the sharp localized contact of the G.H.F. is entirely absent. The failure of the isotropic first-order smoothed resistivity inversion to resolve these distinct geometries clearly underscores the necessity of implementing the structurally constrained inversion step, which utilizes the superior resolution of the seismic models (i.e., V_p, Q) as prior guiding information.

The final, high-resolution electrical resistivity models for all three scenarios are shown in Fig. 12, demonstrating the success of the structurally constrained multi-physics approach. The

sequential inversions in this study were implemented region-wise, and a specific inter-region constraint was applied at the boundary between the seawater and the hemipelagic mud layer. Rather than setting the constraint weight to zero, which would impose a 100% sharp boundary, a non-zero weight was maintained to account for the seawater layer perturbation, leading to more realistic electrical resistivity models. This effect is visible in the results, where the influence of the seawater region causes a decrease in resistivity that extends into the upper subsurface layer. Furthermore, the interface constraint weight of the structural constraints themselves was carefully set to 0.1 (not zero) to account for inherent uncertainty in the derived constraints by 10%, thereby preventing artificial sharpness. For the G.H.F. case (Fig. 12a), the structurally constrained ρ model successfully recovers the sharp boundaries and the high-resistivity contrast of the deep, narrow anomaly, which the unconstrained isotropic inversion failed to delineate. The G.H.P. case (Fig. 12b) accurately resolves the laterally extensive, moderate-to-high resistivity layer characteristic of pore-filling saturation, achieving significantly sharper layer boundaries than the initial model. The composite case (Fig. 12c) provides the most comprehensive validation, demonstrating the method's ability to simultaneously and distinctly delineate both the localized, high-resistivity G.H.F. anomaly and the broader, more diffuse G.H.P. layer.

The final step in this study would be analyzing the resolution and reliability of the seismic inversions involves examining the data density and ray coverage. Figure 13 presents density plots showing the total number of seismic rays (from both traveltime and attenuation surveys) that have traversed each cell of the unstructured mesh for the three synthetic cases. These plots confirm that the survey design provides adequate and consistent illumination across the zones of interest for all scenarios.

5. Conclusion

This study successfully demonstrated the utility of a structurally constrained multi-physics inversion approach for accurately characterizing complex gas-hydrate reservoirs. By utilizing high-resolution seismic models (V_p and Q) to impose structural constraints on the more diffusive electrical resistivity (ρ) model, the method was able to overcome the limitations of isotropic first-order smoothness constrained regularization. The results across three distinct synthetic scenarios — Fracture-Filling (G.H.F.), Pore-Filling (G.H.P.), and Composite —showed that sharp boundaries and complex coexisting structures could be recovered with high fidelity, achieving strong statistical convergence ($\chi_N^2 \approx 1$ and rRMS error < 10%) in all cases. This methodology offers a significant improvement in reservoir delineation, particularly for high-aspect-ratio features that challenge conventional geophysical imaging.

Based on these findings, several avenues can be suggested for future related research to further enhance reservoir characterization. Moving beyond structural constraints, future studies should explore structurally coupled inversion or full joint inversion methods, such as cross-gradient or petrophysical joint inversion, for a truly integrated resolution enhancement across all models. Integrating empirical petrophysical and hydrogeophysical relations is essential. Future research should focus on the development of secondary petrophysical models—such as porosity and water saturation—to refine estimates of hydrate saturation. Additionally, integrating key reservoir

parameters, including hydraulic permeability and seawater salinity, will be essential for advancing the physical realism of reservoir simulations. The adoption of full-waveform inversion (FWI) in seismic imaging is also recommended, given its capability to deliver higher-resolution velocity models and more robust quantitative updates compared to conventional traveltime and amplitude attenuation approaches. Consequently, FWI can yield more reliable structural constraints, which may subsequently be applied to other geophysical properties (e.g., electrical resistivity) to enhance resolution and delineate sharp lithological boundaries with greater confidence.

CRediT authorship contribution statement

Amir Yazdanpanah: Writing – original draft, Methodology, Coding, Visualization, Investigation. Maysam Abedi: Supervision, Methodology, Writing – review & editing.

Declaration of competing interest

The authors declare that they have no known competing financial interests or personal relationships that could have appeared to influence the work reported in this research.

Acknowledgements

We would like to express our sincere thanks to the School of Mining Engineering at the University of Tehran for providing an excellent academic environment and the resources necessary to complete this research. We are particularly grateful to Prof. Dr. Thomas Günther, Chair of Applied Geophysics at TU Bergakademie, Freiberg, Germany, for his invaluable guidance and insightful discussions on various geophysical inversion techniques.

Data availability

Data will be made available on request.

References

Berryman, J. G. (1989). Fermat's principle and nonlinear traveltime tomography. Physical Review Letters, 62(25), 2953–2956. https://doi.org/10.1103/PhysRevLett.62.2953

Bialas, J., Bohlen, T., Dannowski, A., Eisenberg-Klein, G., Gassner, L., Gehrmann, R., Heeschen, K., Hölz, S., Jegen, M., Klaucke, I., Krieger, M., Mann, J., Müller, C., Prüßmann, J., Schicks, J., Schünemann, E., Schwalenberg, K., Sommer, M., Smilde, P. L., … Zander, T. (2020). Joint interpretation of geophysical field experiments in the danube deep-sea fan, Black Sea. Marine and Petroleum Geology, 121, 104551. https://doi.org/10.1016/j.marpetgeo.2020.104551

Böhm, G., Carcione, J. M., Gei, D., Picotti, S., & Michelini, A. (2015). Cross-well seismic and electromagnetic tomography for CO2 detection and monitoring in a saline aquifer. Journal of Petroleum Science and Engineering, 133, 245–257. https://doi.org/10.1016/j.petrol.2015.06.010

Brunet, M., Cook, A., Martin, S., & Mountjoy, J. (2025). Evidence for gas hydrate-filled fractures forming at the sulfate-methane transition zone, Hikurangi subduction margin, New Zealand. Frontiers in Earth Science, 13. https://doi.org/10.3389/feart.2025.1630118

Collett, T. S. (2001). Natural gas hydrates; vast resource, uncertain future. https://doi.org/10.3133/fs02101

Dijkstra, E. W. (1959). A note on two problems in connexion with graphs. Numerische Mathematik, 1(1), 269–271. https://doi.org/10.1007/BF01386390

Doetsch, J., Linde, N., Pessognelli, M., Green, A. G., & Günther, T. (2012). Constraining 3-D electrical resistance tomography with GPR reflection data for improved aquifer characterization. Journal of Applied Geophysics, 78, 68–76. https://doi.org/10.1016/j.jappgeo.2011.04.008

Field, D. A. (2000). Qualitative measures for initial meshes. International Journal for Numerical Methods in Engineering, 47(4), 887–906. https://doi.org/10.1002/(SICI)1097-0207(20000210)47:4<887::AID-NME804>3.0.CO;2-H

Guan, W., Yang, H., Lu, X., & Lu, H. (2024). Pore Characteristics of Hydrate-Bearing Sediments from Krishna-Godavari Basin, Offshore India. Journal of Marine Science and Engineering, 12(10), 1717. https://doi.org/10.3390/jmse12101717

Günther, T., & Rücker, C. (2019). Boundless Electrical Resistivity Tomography BERT 2-the user tutorial version 2.2.8. http://www.pygimli.org

Günther, T., Rücker, C., & Spitzer, K. (2006). Three-dimensional modelling and inversion of dc resistivity data incorporating topography - II. Inversion. Geophysical Journal International, 166(2), 506–517. https://doi.org/10.1111/j.1365-246X.2006.03011.x

Hu, W., Liu, J., Bear, L., & Marcinkovich, C. (2011). A robust and accurate seismic attenuation tomography algorithm. SEG Technical Program Expanded Abstracts 2011, 2727–2731. https://doi.org/10.1190/1.3627760

Hyndman, R. D., Spence, G. D., Chapman, R., Riedel, M., & Edwards, R. N. (2013). Geophysical Studies of Marine Gas Hydrate in Northern Cascadia (pp. 273–295). https://doi.org/10.1029/GM124p0273

Jiang, C., Igel, J., Dlugosch, R., Müller-Petke, M., Günther, T., Helms, J., Lang, J., & Winsemann, J. (2020). Magnetic resonance tomography constrained by ground-penetrating radar for improved hydrogeophysical characterization. GEOPHYSICS, 85(6), JM13–JM26. https://doi.org/10.1190/geo2020-0052.1

Kvenvolden, K. A. (1993). Gas hydrates—geological perspective and global change. Reviews of Geophysics, 31(2), 173–187. https://doi.org/10.1029/93RG00268

Lee, K. H., & Xie, G. (1993). A new approach to imaging with low-frequency electromagnetic fields. Geophysics, 58(6), 780–796. https://doi.org/10.1190/1.1443464

Lei, L., Park, T., Jarvis, K., Pan, L., Tepecik, I., Zhao, Y., Ge, Z., Choi, J.-H., Gai, X., Galindo-Torres, S. A., Boswell, R., Dai, S., & Seol, Y. (2022). Pore-scale observations of natural hydrate-bearing sediments via pressure core sub-coring and micro-CT scanning. Scientific Reports, 12(1), 3471. https://doi.org/10.1038/s41598-022-07184-6

Li, Y., & Oldenburg, D. W. (1996). 3-D inversion of magnetic data. Geophysics, 61(2), 394–408. https://doi.org/10.1190/1.1443968

Liu, T., Liu, X., & Zhu, T. (2020). Joint analysis of P-wave velocity and resistivity for morphology identification and quantification of gas hydrate. Marine and Petroleum Geology, 112, 104036. https://doi.org/10.1016/j.marpetgeo.2019.104036

Liu, Y., Zou, C., Chen, Q., Zhao, J., Li, Y., Sun, J., Liu, C., Peng, C., & Wu, C. (2022). Cross-hole electrical resistivity tomography as an aid in monitoring marine gas hydrate reservoirs for gas recovery: an experimental simulation study. Geophysical Journal International, 233(1), 195–210. https://doi.org/10.1093/gji/ggac454

MATSUMOTO, R. (2009). Overview of Gas Hydrate. Journal of Geography (Chigaku Zasshi), 118(1), 7–42. https://doi.org/10.5026/jgeography.118.7

Miyairi, M., Akihisa, K., Uchida, T., Collett, T. S., & Dallimore, S. R. (1999). Well-log interpretation of gas-hydrate-bearing formations in the JAPEX/JNOC/GSC Mallik 2L-38 gas hydrate research well. https://doi.org/10.4095/210771

Mollaret, C., Wagner, F. M., Hilbich, C., Scapozza, C., & Hauck, C. (2020). Petrophysical Joint Inversion Applied to Alpine Permafrost Field Sites to Image Subsurface Ice, Water, Air, and Rock Contents. Frontiers in Earth Science, 8. https://doi.org/10.3389/feart.2020.00085

Moridis, G. J. . J., Collett, T. S. . S., Pooladi-Darvish, M. ., Hancock, S. ., Santamarina, C. ., Boswell, R. ., Kneafsey, T. ., Rutqvist, J. ., Kowalsky, M. B. . B., Reagan, M. T. . T., Sloan, E. D. . D., Sum, A. K. . K., & Koh, C. A. . A. (2011). Challenges, Uncertainties, and Issues Facing Gas Production From Gas-Hydrate Deposits. SPE Reservoir Evaluation & Engineering, 14(01), 76–112. https://doi.org/10.2118/131792-PA

Moser, T. J. (1991). Shortest path calculation of seismic rays. GEOPHYSICS, 56(1), 59–67. https://doi.org/10.1190/1.1442958

Omisore, B. O., Fayemi, O., Brantson, E. T., Jin, S., & Ansah, E. (2022). Three-dimensional anisotropy modelling and simulation of gas hydrate borehole-to-surface responses. Journal of Natural Gas Science and Engineering, 106, 104738. https://doi.org/10.1016/j.jngse.2022.104738

Pratt, R. G., Bauer, K., & Weber, M. (2003). Crosshole waveform tomography velocity and attenuation images of arctic gas hydrates. SEG Technical Program Expanded Abstracts 2003, 2255–2258. https://doi.org/10.1190/1.1817798

Quan, Y., & Harris, J. M. (1997). Seismic attenuation tomography using the frequency shift method. Geophysics, 62(3), 895–905. https://doi.org/10.1190/1.1444197

Riedel, M., Willoughby, E. C., & Chopra, S. (2010). Geophysical Characterization of Gas Hydrates. Society of Exploration Geophysicists. https://doi.org/10.1190/1.9781560802197

Rücker, C., Günther, T., & Wagner, F. M. (2017). pyGIMLi: An open-source library for modelling and inversion in geophysics. Computers and Geosciences, 109, 106–123. https://doi.org/10.1016/j.cageo.2017.07.011

Ruppel, C. D. (2018). Gas hydrate in nature. https://doi.org/10.3133/fs20173080

Shi, Z., & Wang, C. (2024). Near-surface imaging by joint inversion of ERT and seismic traveltime data with guided FCM clustering. Journal of Applied Geophysics, 222, 105332. https://doi.org/10.1016/j.jappgeo.2024.105332

Taillandier, C., Noble, M., Chauris, H., & Calandra, H. (2009). First-arrival traveltime tomography based on the adjoint-state method. Geophysics, 74(6), WCB1–WCB10. https://doi.org/10.1190/1.3250266

Tanner, D. C., Buness, H., Igel, J., Günther, T., Gabriel, G., Skiba, P., Plenefisch, T., Gestermann, N., & Walter, T. R. (2020). Fault detection. In Understanding Faults (pp. 81–146). Elsevier. https://doi.org/10.1016/B978-0-12-815985-9.00003-5

Tikhonov, A.N., Arsenin, V.Y., 1977. Solutions of Ill-Posed Problems. Winston.

Tong, P., Zhao, D., Yang, D., Yang, X., Chen, J., & Liu, Q. (2014). Wave-equation-based travel-time seismic tomography – Part 1: Method. Solid Earth, 5(2), 1151–1168. https://doi.org/10.5194/se-5-1151-2014

Tryggvason, A., Schmelzbach, C., & Juhlin, C. (2009). Traveltime tomographic inversion with simultaneous static corrections — Well worth the effort. Geophysics, 74(6), WCB25–WCB33. https://doi.org/10.1190/1.3240931

Vasheghani Farahani, M., Hassanpouryouzband, A., Yang, J., & Tohidi, B. (2021). Development of a coupled geophysical–geothermal scheme for quantification of hydrates in gas hydrate-

bearing permafrost sediments. Physical Chemistry Chemical Physics, 23(42), 24249–24264. https://doi.org/10.1039/D1CP03086H

Watanabe, T., & Sassa, K. (1996). Seismic attenuation tomography and its application to rock mass evaluation. International Journal of Rock Mechanics and Mining Sciences & Geomechanics Abstracts, 33(5), 467–477. https://doi.org/10.1016/0148-9062(96)00005-8

Weitemeyer, K., Constable, S., & Key, K. (2006). Marine EM techniques for gas-hydrate detection and hazard mitigation. The Leading Edge, 25(5), 629–632. https://doi.org/10.1190/1.2202668

Wunderlich, T., Fischer, P., Wilken, D., Hadler, H., Erkul, E., Mecking, R., Günther, T., Heinzelmann, M., Vött, A., & Rabbel, W. (2018). Constraining electric resistivity tomography by direct push electric conductivity logs and vibracores: An exemplary study of the Fiume Morto silted riverbed (Ostia Antica, western Italy). GEOPHYSICS, 83(3), B87–B103. https://doi.org/10.1190/geo2016-0660.1

Xin, K., Hung, B., Birdus, S., & Sun, J. (2008). 3-D tomographic amplitude inversion for compensating amplitude attenuation in the overburden. SEG Technical Program Expanded Abstracts 2008, 3239–3243. https://doi.org/10.1190/1.3064018

Yu, L., & Edwards, R. N. (1997). On crosswell diffusive time-domain electromagnetic tomography. Geophysical Journal International, 130(2), 449–459. https://doi.org/10.1111/j.1365-246X.1997.tb05660.x

Figure Captions

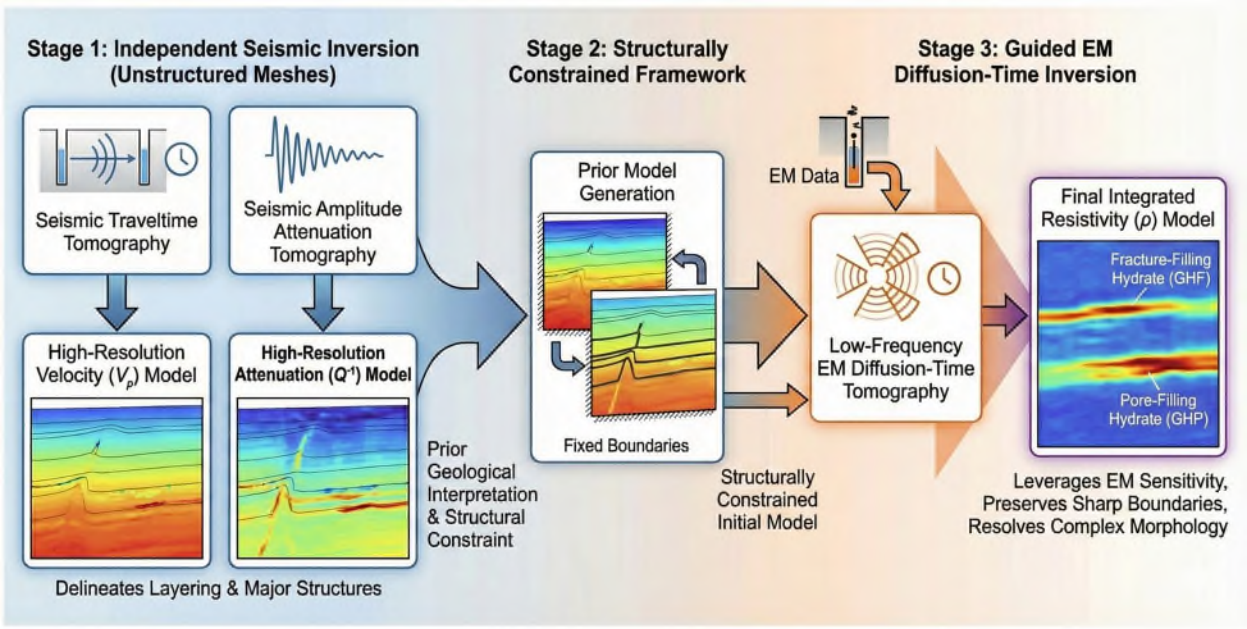


Fig. 1 Workflow of structurally constrained electromagnetic data inversion through cross-borehole seismic and amplitude attenuation survey.

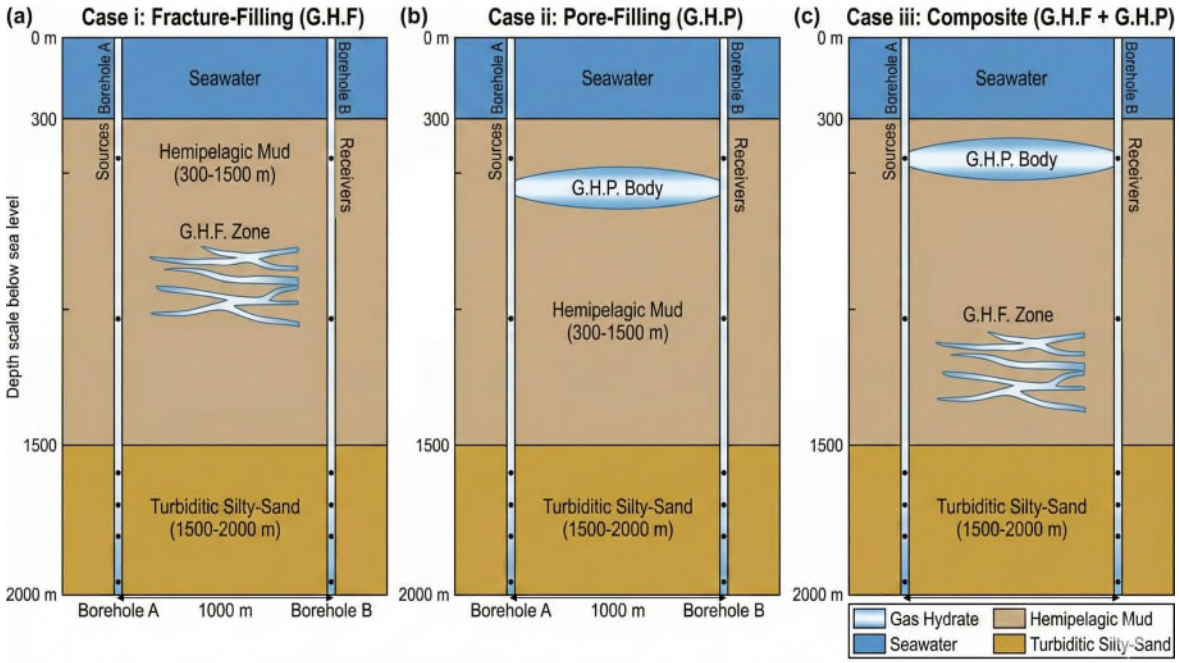


Fig. 2 Schematic representation of the three synthetic gas hydrate reservoir models used for cross-well simulation. (a) Single Fracture-Filling Hydrate (G.H.F.); (b) Single Pore-Filling Hydrate (G.H.P.); and (c) Composite scenario featuring both G.H.F. and G.H.P. (Depth range: 0–2000 m).

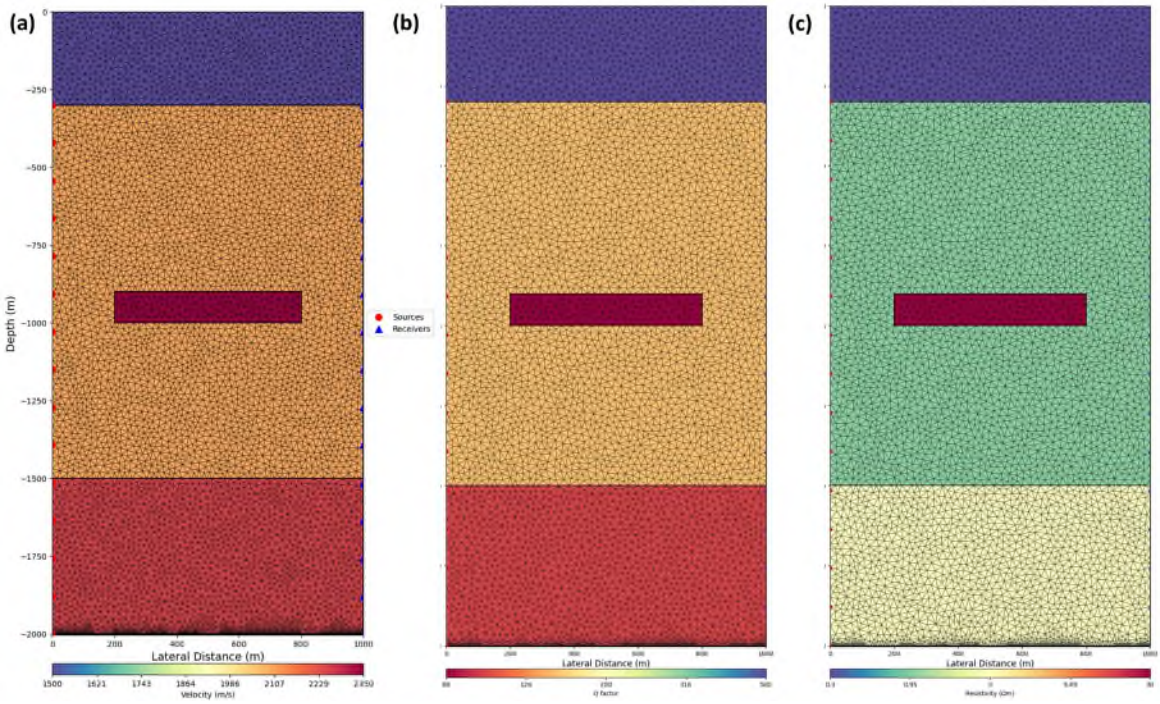
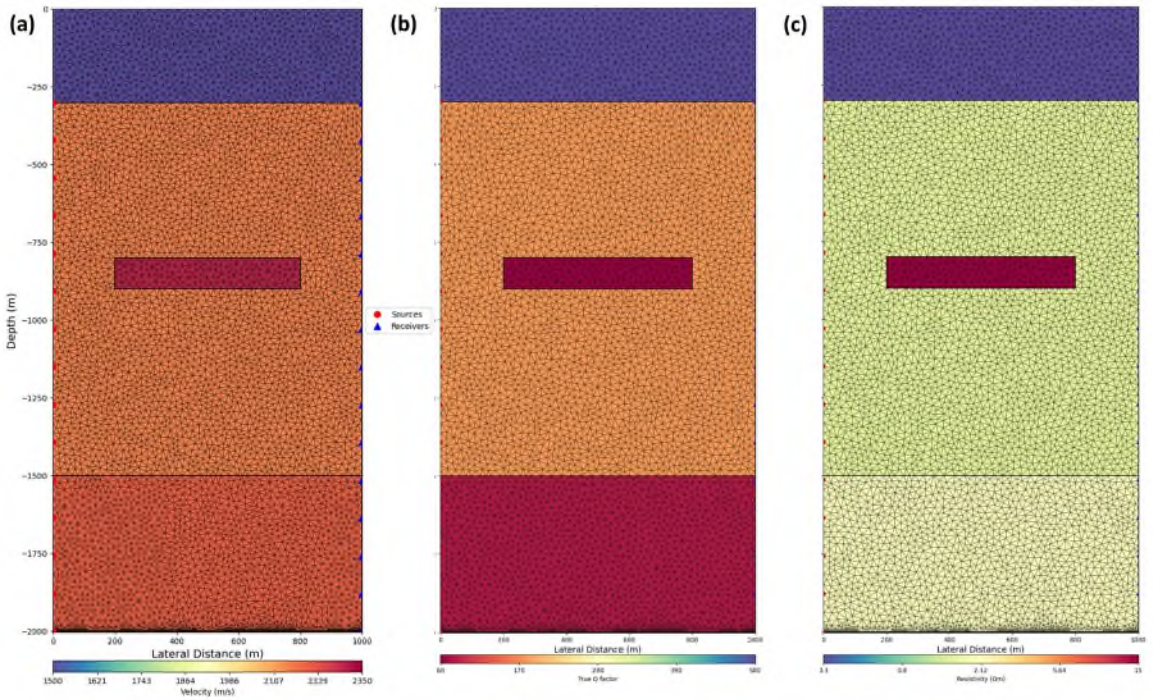


Fig. 3 Reference forward models for the Fracture-Filling Gas Hydrate (G.H.F.) scenario overlaid with fine triangular mesh implemented in forward modeling. (a) P-Wave Velocity (V_p), showing a high-velocity anomaly; (b) Seismic Quality Factor (Q), highlighting the high amplitude attenuation (low Q) of the fractured zone; and (c) Electrical Resistivity (ρ), illustrating the sharp, high-resistivity contrast.



644 **Fig. 4** Reference forward models for the Pore-Filling Gas Hydrate (G.H.P.) scenario overlaid with fine
645 triangular mesh implemented in forward modeling. (a) P-Wave Velocity (V_p), showing a high-velocity
646 anomaly; (b) Seismic Quality Factor (Q), highlighting the high amplitude attenuation (low Q) of the
647 fractured zone; and (c) Electrical Resistivity (ρ), illustrating the sharp, high-resistivity contrast.

648

649

650

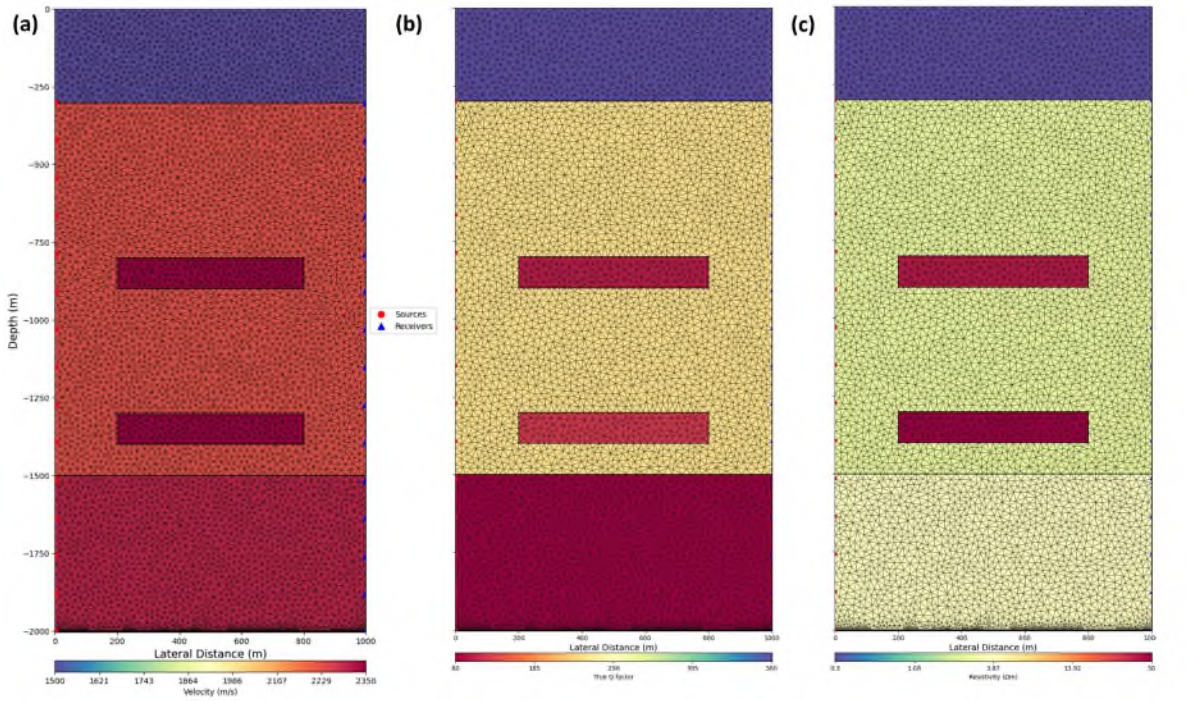


Fig. 5 Reference forward models for the Composite (G.H.F. & G.H.P.) scenario overlaid with fine triangular mesh implemented in forward modeling. (a) P-Wave Velocity (V_p), showing a high-velocity anomaly; (b) Seismic Quality Factor (Q), highlighting the high amplitude attenuation (low Q) of the fractured zone; and (c) Electrical Resistivity (ρ), illustrating the sharp, high-resistivity contrast.

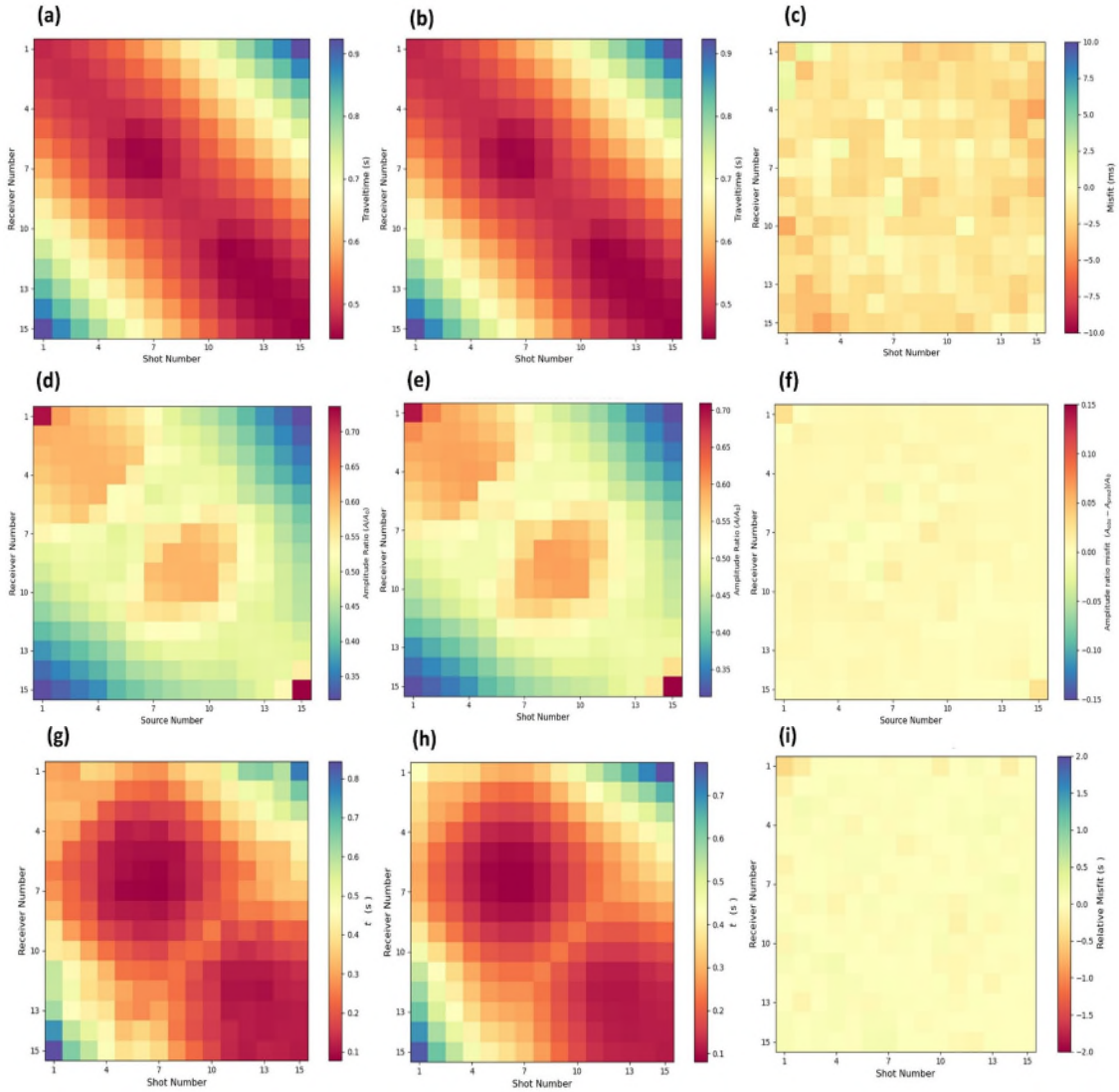


Fig. 6 Multi-Physics Data, Predictions, and Misfits for the Fracture-Filling Hydrate (G.H.F.) Scenario. (a-c) Seismic Travel Time Data (t): Observed data (a), predicted data (b), and the absolute misfit (c) between the observed and predicted travel times; (d-f) Seismic Amplitude Attenuation Data ($ln(A/A_0)$): Observed data (d), predicted data (f), and the absolute misfit (f) for the logarithm of the normalized amplitude ratio, which is proportional to the total attenuation. (g-i) EM Diffusion Time Data (t_{EM}): Observed data (g), predicted data (h), and the relative misfit (i) for the square root of the geometrical diffusion time.

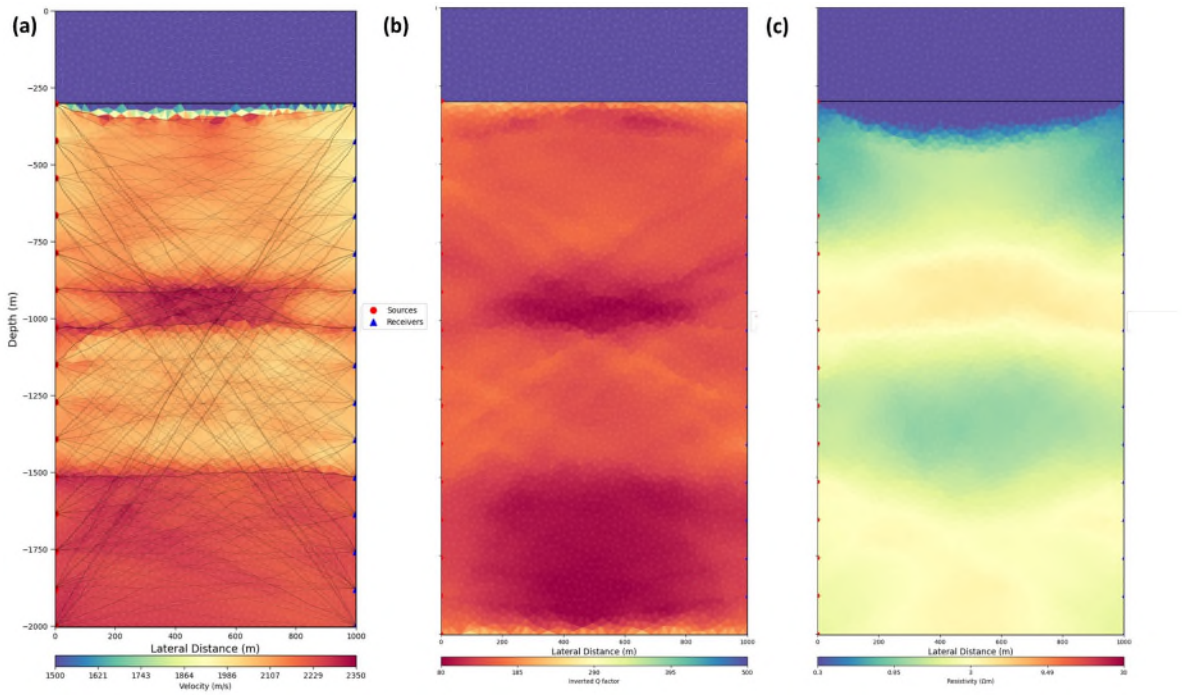
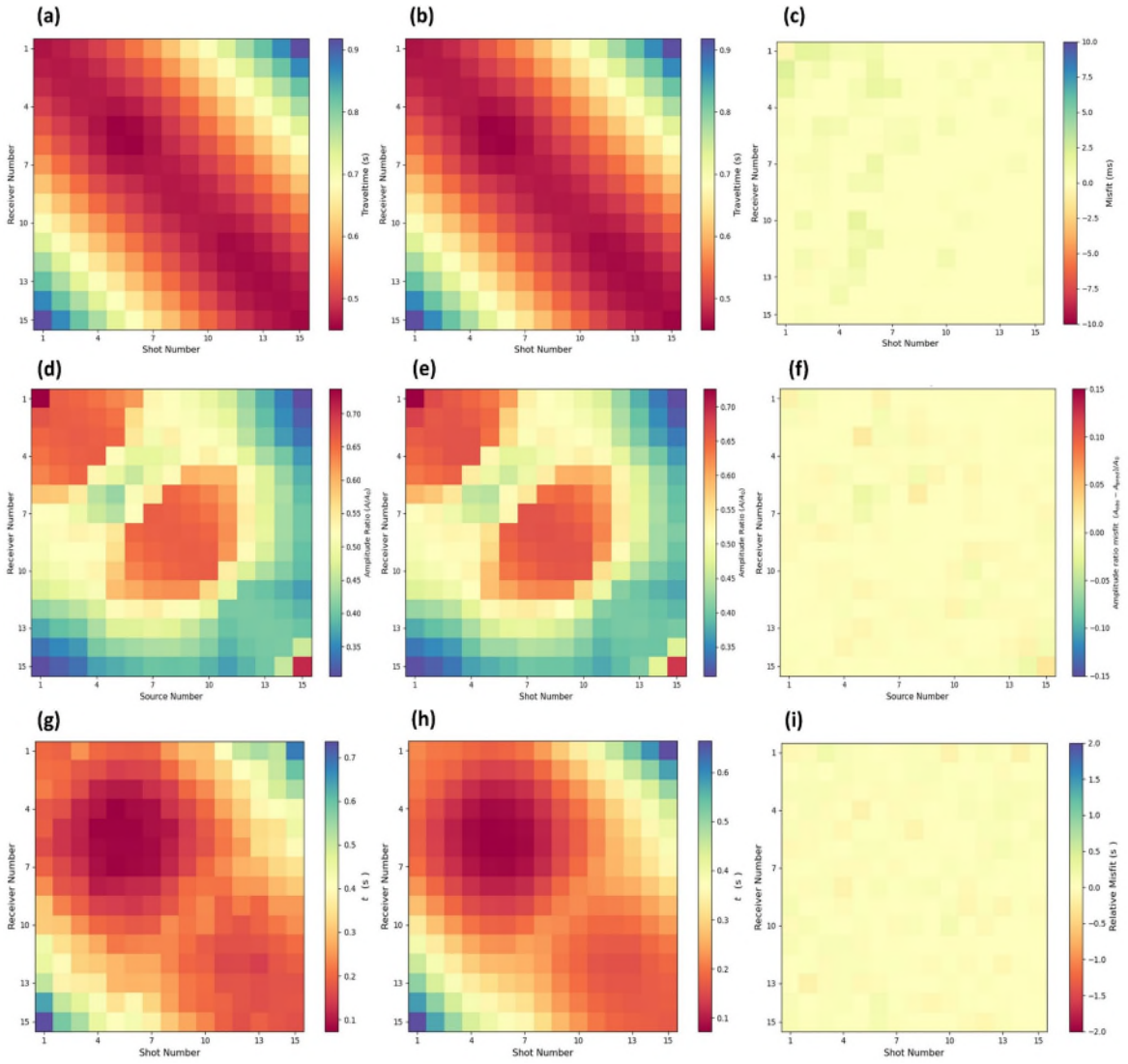


Fig. 7 Inversion Results for the Fracture-Filling Hydrate (G.H.F.) Scenario. (a) P-Wave Velocity (V_p): Inversion result from seismic traveltime tomography, effectively delineating the high-velocity G.H.F. zone and background layering; (b) Attenuation Factor (Q^{-1}): Inversion result from seismic amplitude attenuation tomography, showing the highly dissipative nature of the fracture zone; (c) Electrical Resistivity (ρ): Primary Inversion Result from the electromagnetic geometrical diffusion time tomography. This initial model was generated using a standard isotropic smoothness constraint and serves as the starting point, along with the results from (a) and (b), for the subsequent structurally constrained inversion.



685 **Fig. 8** Multi-Physics Data, Predictions, and Misfits for the Pore-Filling Hydrate (G.H.P.) Scenario. (a-c)
686 Seismic Travel Time Data (t): Observed data (a), predicted data (b), and the absolute misfit (c) between
687 the observed and predicted travel times; (d-f) Seismic Amplitude Attenuation Data ($ln(A/A_0)$): Observed
688 data (d), predicted data (f), and the absolute misfit (f) for the logarithm of the normalized amplitude ratio,
689 which is proportional to the total attenuation. (g-i) EM Diffusion Time Data (t_{EM}): Observed data (g),
690 predicted data (h), and the relative misfit (i) of the geometrical diffusion time.

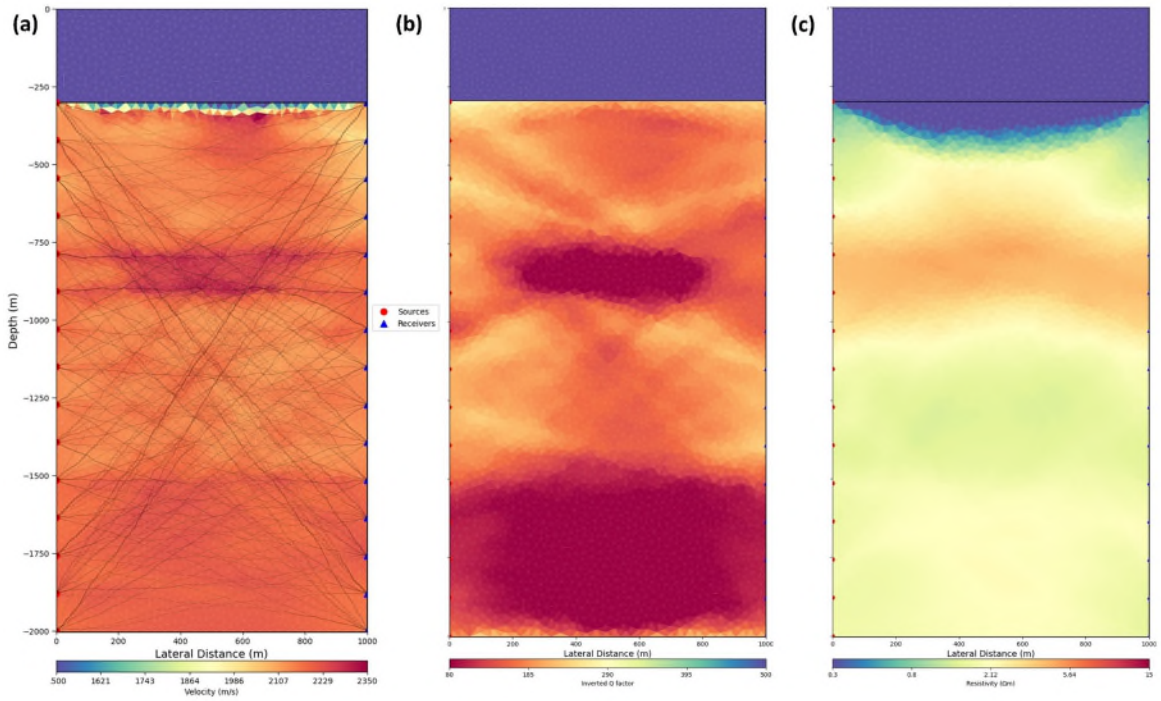


Fig. 9 Inversion Results for the Pore-Filling Hydrate (G.H.P.) Scenario. (a) P-Wave Velocity (V_p): Inversion result from seismic traveltime tomography, effectively delineating the high-velocity G.H.F. zone and background layering; (b) Attenuation Factor (Q^{-1}): Inversion result from seismic amplitude attenuation tomography, showing the highly dissipative nature of the pore zone; (c) Electrical Resistivity (ρ): Primary Inversion Result from the electromagnetic geometrical diffusion time tomography. This initial model was generated using a standard isotropic smoothness constraint and serves as the starting point, along with the results from (a) and (b), for the subsequent structurally constrained inversion.

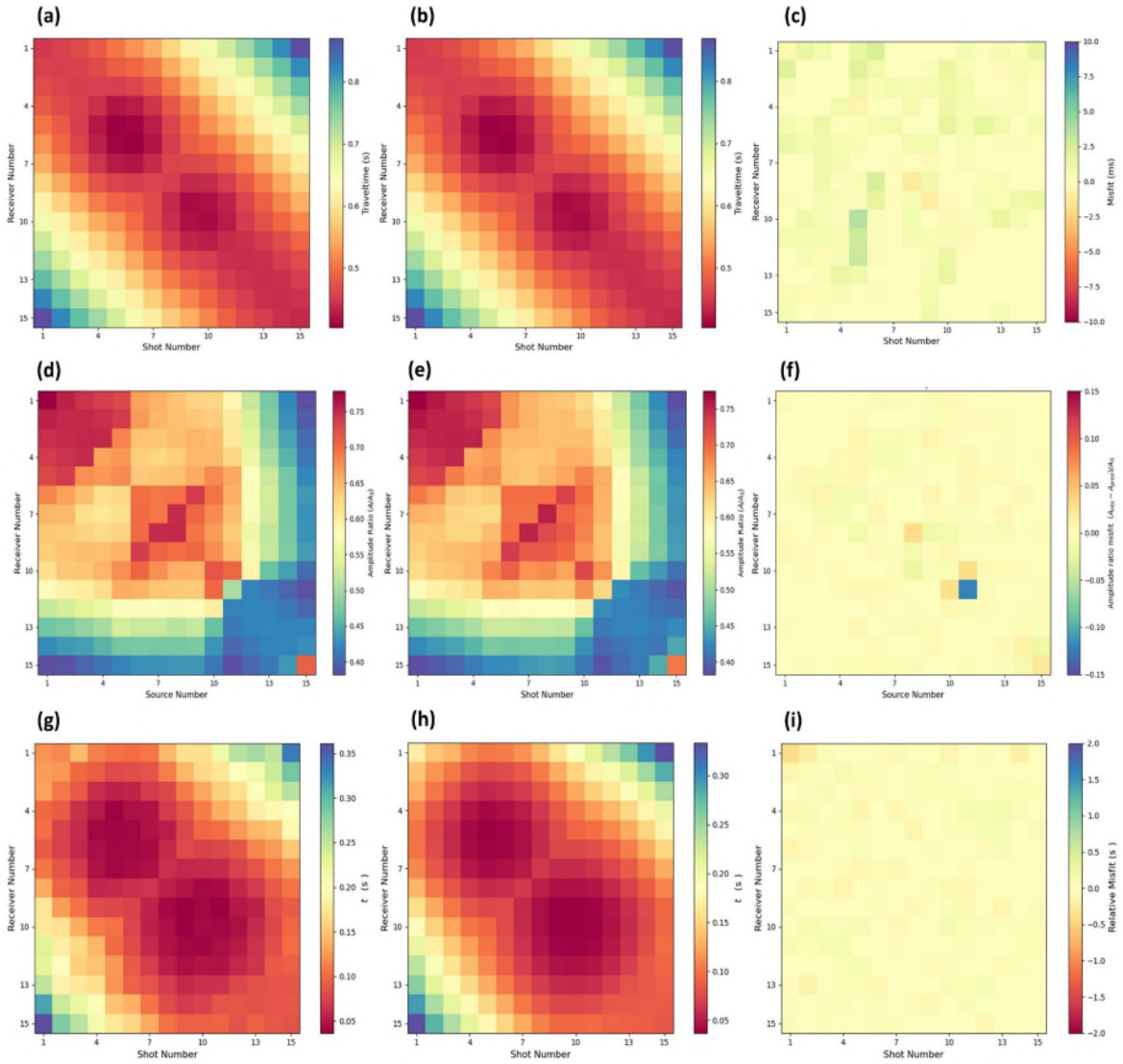


Fig. 10 Multi-Physics Data, Predictions, and Misfits for the Composite Gas-Hydrate (G.H.F. & G.H.P.) Scenario. (a-c) Seismic Travel Time Data (t): Observed data (a), predicted data (b), and the absolute misfit (c) between the observed and predicted travel times; (d-f) Seismic Amplitude Attenuation Data ($ln(A/A_0)$): Observed data (d), predicted data (f), and the absolute misfit (f) for the logarithm of the normalized amplitude ratio, which is proportional to the total attenuation. (g-i) EM Diffusion Time Data (t_{EM}): Observed data (g), predicted data (h), and the relative misfit (i) of the geometrical diffusion time.

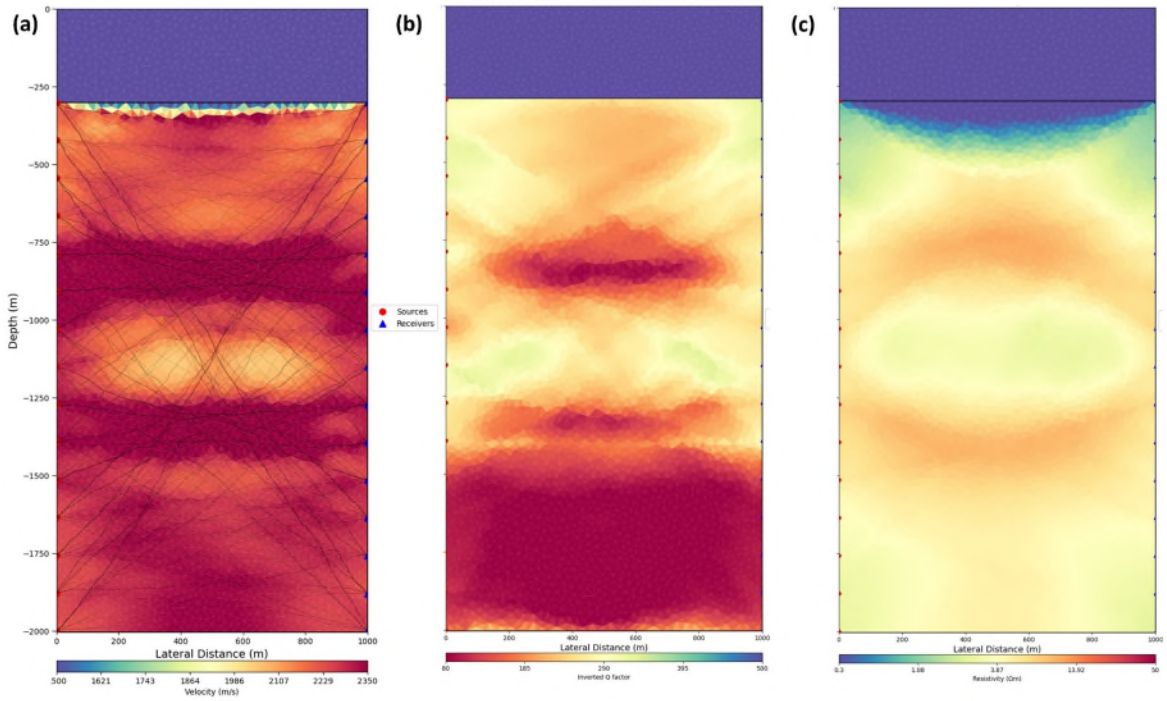


Fig. 11 Inversion Results for the Composite Gas-Hydrate (G.H.F. & G.H.P.) Scenario. (a) P-Wave Velocity (V_p): Inversion result from seismic traveltime tomography, effectively delineating the high-velocity G.H.F. zone and background layering; (b) Attenuation Factor (Q^{-1}): Inversion result from seismic amplitude attenuation tomography, showing the highly dissipative nature of the pore zone; (c) Electrical Resistivity (ρ): Primary Inversion Result from the electromagnetic geometrical diffusion time tomography. This initial model was generated using a standard isotropic smoothness constraint and serves as the starting point, along with the results from (a) and (b), for the subsequent structurally constrained inversion.

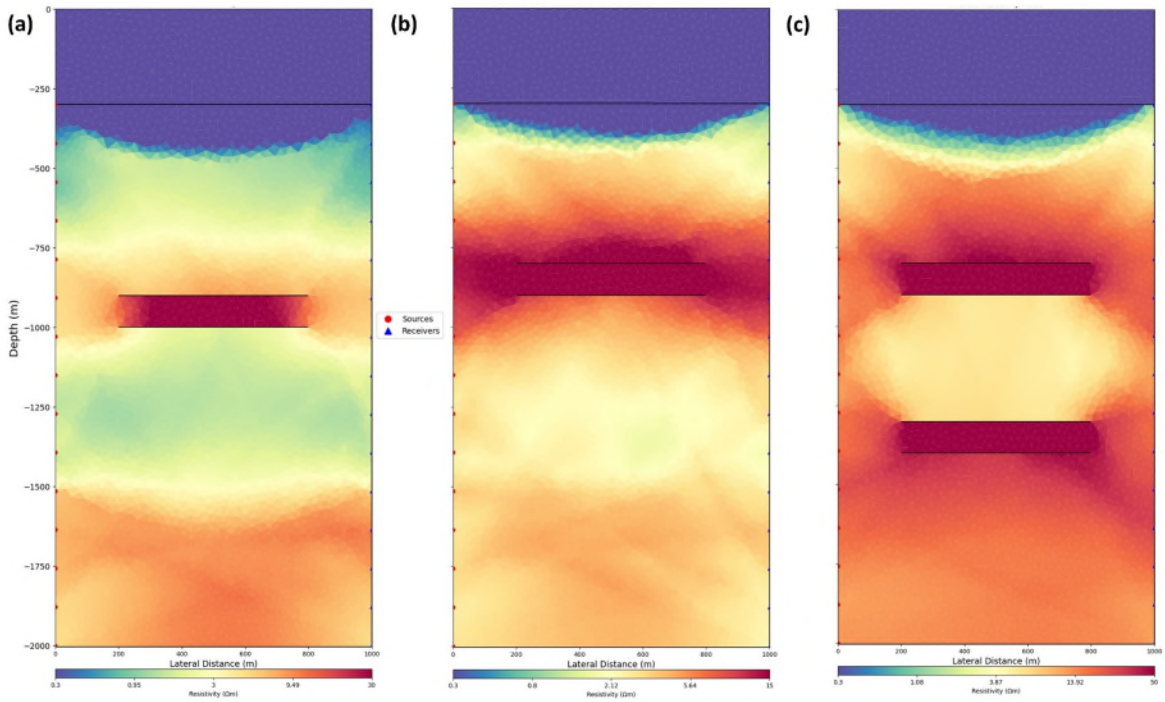


Fig. 12 Final Structurally Constrained Electrical Resistivity Inversion Results. (a) Fracture-Filling Hydrate (G.H.F.), Final constrained ρ model, showing the recovery of the sharp boundaries and high-resistivity contrast of the near-vertical fracture zone; (b) Pore-Filling Hydrate (G.H.P.), Final constrained ρ model, accurately resolving the laterally extensive, moderate-to-high resistivity layer characteristic of pore-filling saturation; (c) Composite Case (G.H.F. and G.H.P.), Final constrained ρ model, demonstrating the method's ability to simultaneously delineate both the sharp, high-resistivity fracture and the broader, more diffuse pore-filling layer.

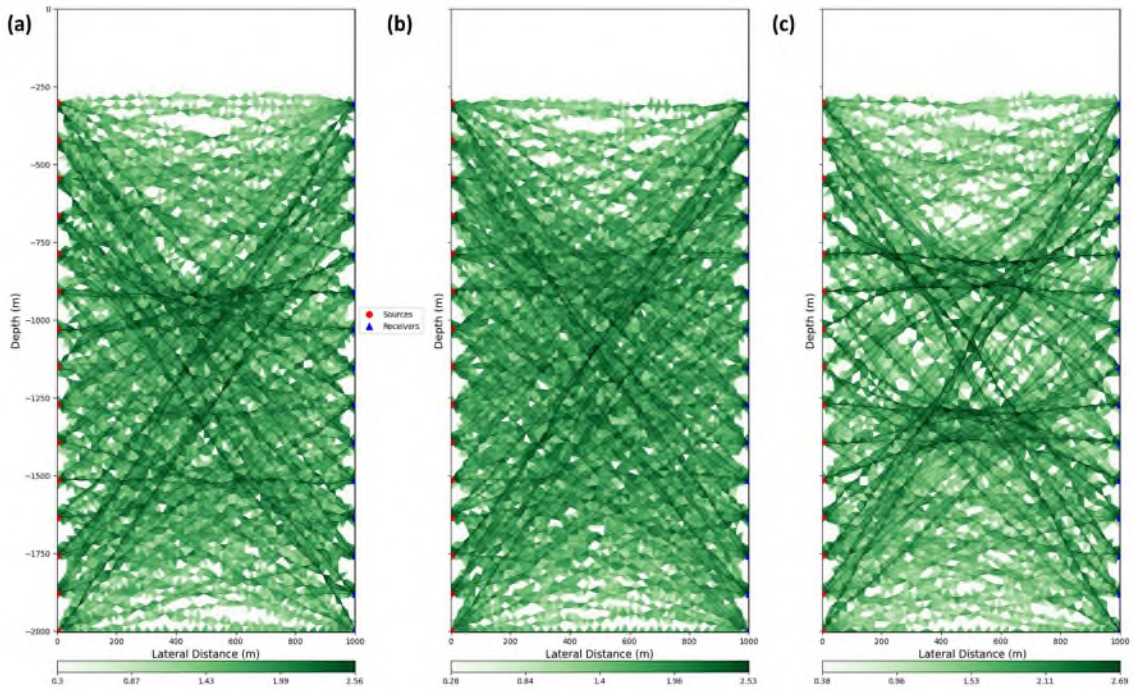


Fig. 13 Density plots showing the total number of seismic rays (from both traveltime and attenuation surveys) that have traversed each cell of the unstructured mesh for the three synthetic reservoir cases; (a) G.H.F. Case, Ray coverage plot demonstrating high resolution and intersecting coverage across the central zone between the boreholes. (b) G.H.P. Case, Ray coverage plot detailing the data density across the shallower, horizontally extensive target layer. (c) Composite Case, Ray coverage plot reflecting the combined ray path density needed to image both the shallow pore-filling and the deeper fracture-filling targets.

Table Captions

Table. 1 Geophysical and Geological Properties of Fracture-Filling test reservoir.

Layer/Unit	Material	Thickness/Depth (m)	P-Wave Velocity (m/s)	Quality Factor (-)	Electrical Resistivity (Ωm)	Dip	Volume Fraction
Layer 1	Seawater	300 (0-300)	1500	500	0.3	-	-
Layer 2	hemipelagic mud-rich sediment	1200 (300-1500)	2100	150	1	-	-
Layer 3	turbiditic silty-sand	500 (1500-2000)	2250	100	3	-	-
Anomaly	Fracture-filling massive Gas Hydrate	100 (900-1000)	2350	80	30	Horizontal fractures ≤20°	0.6

766 **Table. 2** Geophysical and Geological Properties of Pore-Filling test reservoir.

Layer/Unit	Material	Thickness/Depth (m)	P-Wave Velocity (m/s)	Quality Factor (-)	Electrical Resistivity (Ωm)	Dip	Volume Fraction
Layer 1	Seawater	300 (0-300)	1500	500	0.3	-	-
Layer 2	hemipelagic mud-rich sediment	1200 (300-1500)	2150	180	1.5	-	-
Layer 3	turbiditic silty-sand	500 (1500-2000)	2200	80	2	-	-
Anomaly	Hydrate-bearing Silty-Sand (Pore-filling)	100 (800-900)	2300	60	15	-	0.4

767

768

769

770

771

772

773

774

775

776

777

778

779

780

781

782

783

784 **Table. 3** Geophysical and Geological Properties of Composite test reservoir.

Layer/Unit	Material	Thickness/Depth (m)	P-Wave Velocity (m/s)	Quality Factor (-)	Electrical Resistivity (Ωm)	Dip	Volume Fraction
Layer 1	Seawater	300 (0-300)	1500	500	0.3	-	-
Layer 2	hemipelagic mud-rich sediment	1200 (300-1500)	2225	250	2.5	-	-
Layer 3	turbiditic silty-sand	500 (1500-2000)	2300	80	4	-	-
Anomaly 1	Hydrate-bearing Silty-Sand	100 (800-900)	2700	100	40	-	0.5
Anomaly 2	Fracture-filling massive Gas Hydrate	100 (1300-1400)	2600	120	50	Horizontal fractures ≤20°	0.7

785

786